Polymer Testing 106 (2022) 107443

Contents lists available at ScienceDirect

Polymer Testing

journal homepage: www.elsevier.com/locate/polytest

Systematic analysis and nanoscale chemical imaging of polymers using photothermal-induced resonance (AFM-IR) infrared spectroscopy

A. Catarina V.D. dos Santos, Bernhard Lendl **, Georg Ramer *

Institute of Chemical Technologies and Analytics, TU Wien, 1060, Vienna, Austria

ARTICLE INFO

Keywords:
AFM-IR
Chemical characterization
Polymer analysis
Nanoscale infrared spectroscopy

ABSTRACT

In this work, a reliable and time-saving protocol for the measurement of polymers using photothermal-induced resonance (AFM-IR) at the nanoscale was developed and applied to 4 industrially relevant polymers: a polypropylene-based reactor thermoplastic polyolefin (rTPO), linear low density polyethylene (LLDPE) for molding and two recycled post-consumer polypropylene/polyethylene blends. In addition to the morphology obtained through AFM, we were able to identify and image the major components of each polymer, including the mineral fillers (talc and calcium carbonate) present in each blend using nanoscale spatial resolution infrared imaging. The protocol developed allows the quick analysis and identification at the nanoscale of the major components of a blend without having previous knowledge of the sample composition, a major advantage when compared to other traditionally used imaging techniques such as TEM and SEM.

1. Introduction

Synthetic polymers are a success story: in a little over a century and a half they have gone from a curiosity in the chemistry labs to being omnipresent in day-to-day life [1]. This takeover was driven by the advantages these materials have over traditional ones, such as their lower price, lighter weight, versatility, and durability. Nowadays, in addition to improving performance of polymer materials, polymer recycling and recyclability have gained in importance. For example, the European Union (EU) considers polymer recycling as an important piece of the circular economy action plan, a key element for the success of the European green deal [2] as a way to both reduce the production of new polymers and the percentage of already existing polymers that become waste. In contrast to recycling of inorganic materials polymer recycling poses some additional challenges: there is a limit to the amount of recycling cycles a polymer can go through before it becomes waste, and the presence of contaminants can lead to undesirable blends [3,4].

The nano- and microscale structure and chemical composition of a polymer has great influence on its macroscale properties [5]. It is therefore of great importance, to have methods that allow us to probe into this nano realm and obtain as much information as possible. This information could provide valuable insights into the improvement of recycling and manufacturing processes. The structure of polymers can be analyzed by a variety of methods including mass spectrometry (often hyphenated with chromatographic techniques) [6–8], X-ray diffraction [9,10], transmission electron microscopy (TEM) [11,12], scanning electron microscopy (SEM) [13–15], atomic force microscopy (AFM) [16–18], Raman spectroscopy [19,20], and FTIR [21–23]. Although these techniques provide a great deal of information, they cannot provide explicit chemical analysis at the nanoscale.

AFM-IR, also called PTIR, is a recent technique that allows for infrared spectroscopy to be performed at the nanometer spatial resolution scale [24], a huge advantage when compared to the diffraction-limited mid-IR microscopy which only achieves micrometer spatial resolution [25]. AFM-IR uses the thermal expansion of the sample area underneath the AFM tip caused by the absorption of radiation from a pulsed wavelength-tunable IR laser to achieve spatial resolution significantly below the limit of diffraction.

For the chemical spectroscopist one of the most attractive features of AFM-IR is that it provides spectra that compare well to conventional FTIR absorption spectra, because both the FTIR and AFM-IR signals are proportional to the wavelength dependent absorption coefficient of the sample [26]. The thermal expansion is proportional to the absorbed energy and causes changes in the deflection signal of the AFM cantilever. The signal is thus detected in the near-field, which permits lateral resolutions of up to 20 nm in contact mode and ≈10 nm in tapping mode

* Corresponding author.
** Corresponding author.
E-mail addresses: bernhard.lendl@tuwien.ac.at (B. Lendl), georg.ramer@tuwien.ac.at (G. Ramer).

https://doi.org/10.1016/j.polymertesting.2021.107443
Received 3 November 2021; Accepted 26 November 2021
Available online 27 November 2021

[26,27]. The recent invention of tapping mode AFM-IR makes the method more attractive for polymer analysis [28], as tapping mode AFM-IR is better suited for the analysis of soft and heterogeneous samples (such as polymers), due to the cantilever resonance frequencies being less susceptible to changes in the mechanical properties of the sample when compared to resonance-enhanced contact-mode AFM-IR [29]. This has enabled the application of AFM-IR to various types of samples such as aerosol particles [30,31], semiconductors [32], drug nanocarriers [27,33], metal organic frameworks (MOFs) [34], oil paints [35], viruses [36,37], and cells and intracellular proteins [38–40]. Studies on polymers and their properties have also been reported, namely on polymer structure [41–43], degradation [44–46], and polymer-metal interfaces [47,48], among others.

AFM-IR has also been applied previously to polymers by Tang et al. [49] in their first analysis of the nanodomains present in impact propylene copolymer (IPC) in 2016. In 2018, the researchers complemented this analysis by concluding that the composition of the core in the core-shell rubber particle morphology typical of this polymer is dependent on the polymerization conditions, and can be PE or PP [50]. Despite all of these studies, which are typically focused on answering highly specialized research questions there is still no established protocol for routine reproducible AFM-IR measurements of polymers, a knowledge gap that this work intends to fill. We compiled a five step protocol that include guidelines from sample preparation to interpretation of results. This protocol is then applied to a range of common commercial polymers of the most produced polymer group in Europe in 2019, polyolefins [51]. These include a reactor thermoplastic polyolefin (rTPO), LLDPE, and two recycled PP/PE blends.

Reactor thermoplastic polyolefins (rTPOs), also known as impact copolymers or heterophasic copolymers, consist of a hard semi-crystalline PP or PE matrix and a soft component such as ethylene-propylene rubber (EPR) [52]. rTPOs are produced by co-polymerization of different monomers in several reactors, resulting in a polymer alloy with smaller size of evenly distributed rubber crystals and improved impact strength when compared to those produced by melt compounding [53,54]. It is important to find balance between improving the impact strength and other potentially desirable properties such as stiffness, heat deflection temperature and toughness. One way to achieve this is through the addition of mineral fillers, which can be further fine-tuned by adjusting the concentration and particle size [55]. rTPOs are commonly used in the automotive industry as bumpers and battery cases [56].

Linear low density polyethylene (LLDPE) has a long linear backbone and randomly distributed short side chain branches [52]. LLDPE has higher tensile strength, impact strength, tear resistance, and puncture resistance than low-density polyethylene (LDPE) and has found widespread use in injection molding and blow molding, as well as in films, packaging, cable insulation, and tubing, among others [57–59].

In this work, we take a systematic approach to the analysis of polymers using AFM-IR and present a protocol that leads from an unknown polymer sample to knowledge of its general nanoscale characteristics in one measurement. Care is taken to ensure that the chemical images obtained are not affected by topographic cross-talk. We demonstrate the validity of our protocol by applying it to four commercially available samples and obtaining the chemical distribution of not only its phase domains (when present) but also of the distribution of the mineral fillers and other components. In the recycled post-consumer polymers analyzed it was possible to characterize in detail various phases present.

2. Experimental

2.1. Materials

Hifax CA 7442A from LyondellBasell, a commercially available polypropylene rTPO, and LL 6101 from ExxonMobil, a commercially available LLDPE were provided by Omya. Furthermore, two commercially available recycled PP/PE copolymers containing different mineral fillers from the Skyfil product line were provided by PreZero Polymers: Skyfil 1 (06MT05C15) and Skyfil 2 (06HH06T10).

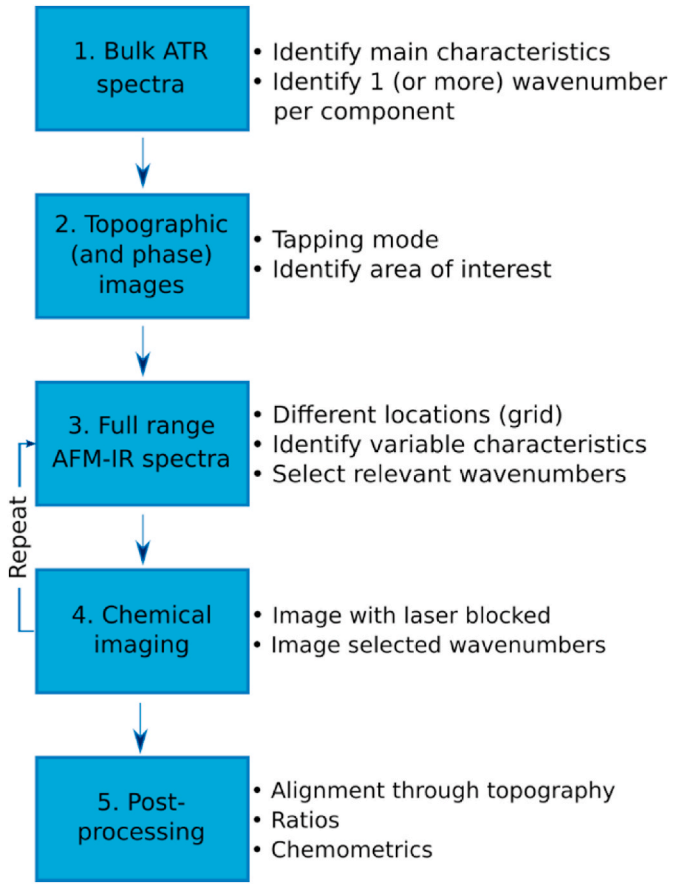

Fig. 1. Protocol for AFM-IR measurements of unknown polymer samples. Steps 3. and 4. can be repeated, if necessary, to obtain optimal chemical imaging.

2.2. ATR-FTIR measurements

ATR FTIR measurements were performed on a Bruker Tensor 37 equipped with a Platinum ATR accessory. The spectra were collected by averaging 8 spectra with 2 cm^{-1} resolution.

2.3. Sample preparation

The samples were ultra-cryomicrotomed at −100 °C on a Leica EM-UC7 equipped with a Leica EM FC7 cryochamber or on a PowerTome PC with CR-X cryosectioning system (Boeckeler Instruments), and the resulting sections were placed on ZnS substrates (13 mm diameter × 1 mm thickness from Crystran).

2.4. AFM-IR measurements

All AFM-IR measurements were carried out using a Bruker nano-IR 3s coupled to a MIRcat-QT external cavity quantum cascade laser array (EC-QCL) from Daylight Solutions. Spectra covering the range from 910 cm^{-1} to 1650 cm^{-1} were obtained using AFM-IR in tapping mode with a heterodyne detection scheme. The measurements were obtained while driving the cantilever at its second resonance frequency ($f_2 \approx 1500$ kHz) and demodulating the AFM-IR signal at the first resonance frequency ($f_1 \approx 250$ kHz) using a digital lock-in amplifier (MFLI from Zurich Instruments). The laser repetition rate was set to $f_L = f_2 - f_1 \approx 1300$ kHz. The cantilevers used were gold coated with nominal first

free resonance frequencies of 300 ± 100 kHz and spring constants between 20 and 75 N/m (Tap300GB-G from BudgetSensors). The laser source operated at 10% duty cycle and 14.8% power (before beam splitter). For each location, 3 spectra were recorded at 1 cm^{-1} spectral resolution. The instrument and all beam paths were purged with dry air generated by an adsorptive dry air generator.

2.5. Data processing

Recorded AFM-IR spectra were averaged by location, normalized to the maximum value in the range between 1400 cm^{-1} and 1500 cm^{-1} and smoothed using a Savitzky-Golay filter (9 points, first order).

The shift between chemical images was corrected using sub pixel registration via phase cross correlation based on their simultaneously recorded topography counterparts as reference. Calculations were performed using the phase cross correlation implementation in the scikit-image package for Python 3 [60].

3. Results and discussion

Key to reproducible and routine AFM-IR polymer characterization is a protocol that can be applied to a wide range of polymer samples. The protocol developed in this study is presented in Fig. 1.

3.1. Bulk ATR spectra (step 1)

The first step of this protocol entails gaining a general mid-IR spectroscopic understanding of the sample. In this study, we chose to take single bulk ATR spectrum to get an overview of the bands present in each material. However, if there are other established sources of information (prior experience, band assignment tables, reference spectra) they can be used instead. Taking a new spectrum of each material is thus optional but recommended, The information obtained will also prove useful in the final optimization steps necessary to start an AFM-IR measurement when using an EC-QCL array, where knowledge of absorption bands in different regions of the spectrum (one for each EC-QCL chip used) is necessary for the final alignment of the mid-IR laser source. Due to the vastly different spatial resolutions achieved in far field IR and AFM-IR, we have found no advantage in taking care to image the same sample area using a far field IR microscope.

3.2. Topography (and phase) images (step 2)

Sample preparation is a critical step to ensure a successful measurement. The polymer samples should be cut with an ultra-(cryo) microtome below their glass-transition temperature (to avoid smearing) into sections with a submicron thickness, as in thicker sections signal saturation may occur [61]. Furthermore, the choice of a reflective substrate (e.g., gold) will have a wavelength-dependent influence on the spectra obtained [61], therefore, we recommend the use of non-reflective IR transparent substrates, such a CaF_2 or ZnSe. These substrates are available commercially as optical windows. The initial part of an AFM-IR measurement is a topographic AFM measurement. For polymer samples tapping mode is preferred over contact mode, since it reduces the possibility of sample damage due to weaker tip-sample interactions [62].

3.3. Full range AFM-IR spectra (step 3)

Once a region of interest is chosen and an AFM image is obtained, the next step is to obtain several AFM-IR spectra in a grid. In this work we have used 4 × 4 grids covering the 10 μm × 10 μm areas imaged, an example of which can be found in Appendix A. This allows us to quickly estimate whether certain bands are present everywhere or only in certain locations. If there are further points of interest visible in the topography, additional spectra can be obtained before selecting which

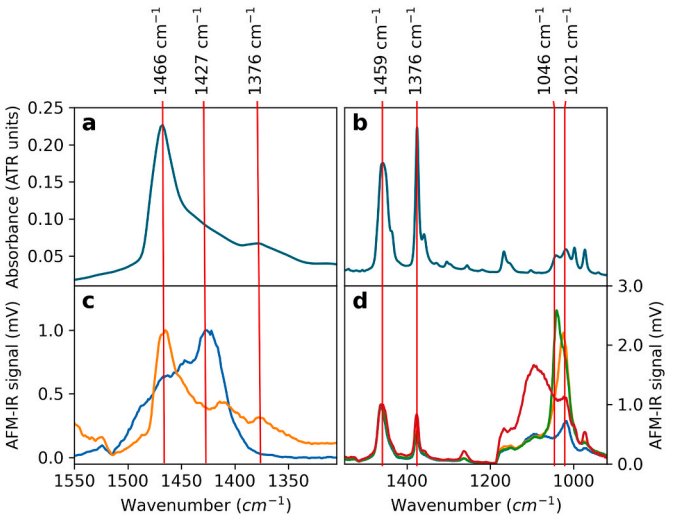

Fig. 2. Comparison of bulk ATR spectra (top row) and AFM-IR spectra (bottom row) obtained in different locations for LLDPE (a,c) and rTPO (b,d). The AFM-IR spectra are normalized to the 1459 cm^{-1} band intensity.

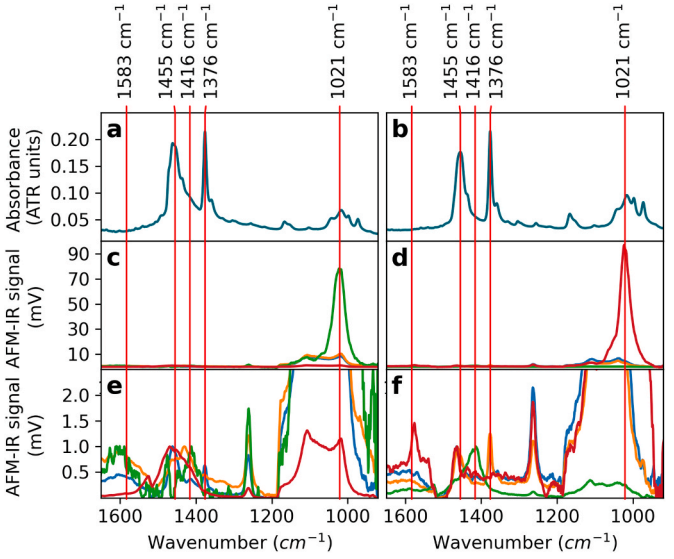

Fig. 3. Comparison of bulk ATR spectra and AFM-IR spectra obtained in different locations for (a), (c), (e) Skyfil 1 and (b), (d), (f) Skyfil 2. (c) and (e), and (d) and (f) correspond to the same spectra but with different scales. The AFM-IR spectra are normalized to the 1459 cm^{-1} band intensity. (*) The peak at 1263 cm^{-1} is present in all the samples analyzed and has been attributed to silicone oil contamination of commercial AFM cantilever tips [66].

wavenumbers to image. The wavelength selection process can vary depending on prior knowledge and sample complexity. For simpler samples (with only a few major components) the identification of the wavenumbers of interest is straightforward. Fig. 2 and Fig. 3 are examples of such selections. However, more complex samples may require chemometric analysis such as clustering or PCA to facilitate the identification of the main features. Examples of the application of chemometrics to the analysis of polymer samples using FTIR are abundant and demonstrate the versatility and usefulness of such approach [63–65]. Figs. 2 and 3 illustrate how the selection of relevant wavenumbers can be performed. In the case of LLDPE (Fig. 2, (a) and (c)) the advantage of AFM-IR over bulk FTIR is clearly visible, as from spectra obtained in two distinct locations it is possible to separately identify the polymer itself (orange), and $CaCO_3$ (blue) with a peak at 1427 cm^{-1}, the filler. Also, for the rTPO (Fig. 2, (b) and (d)) it is possible to separate locations with

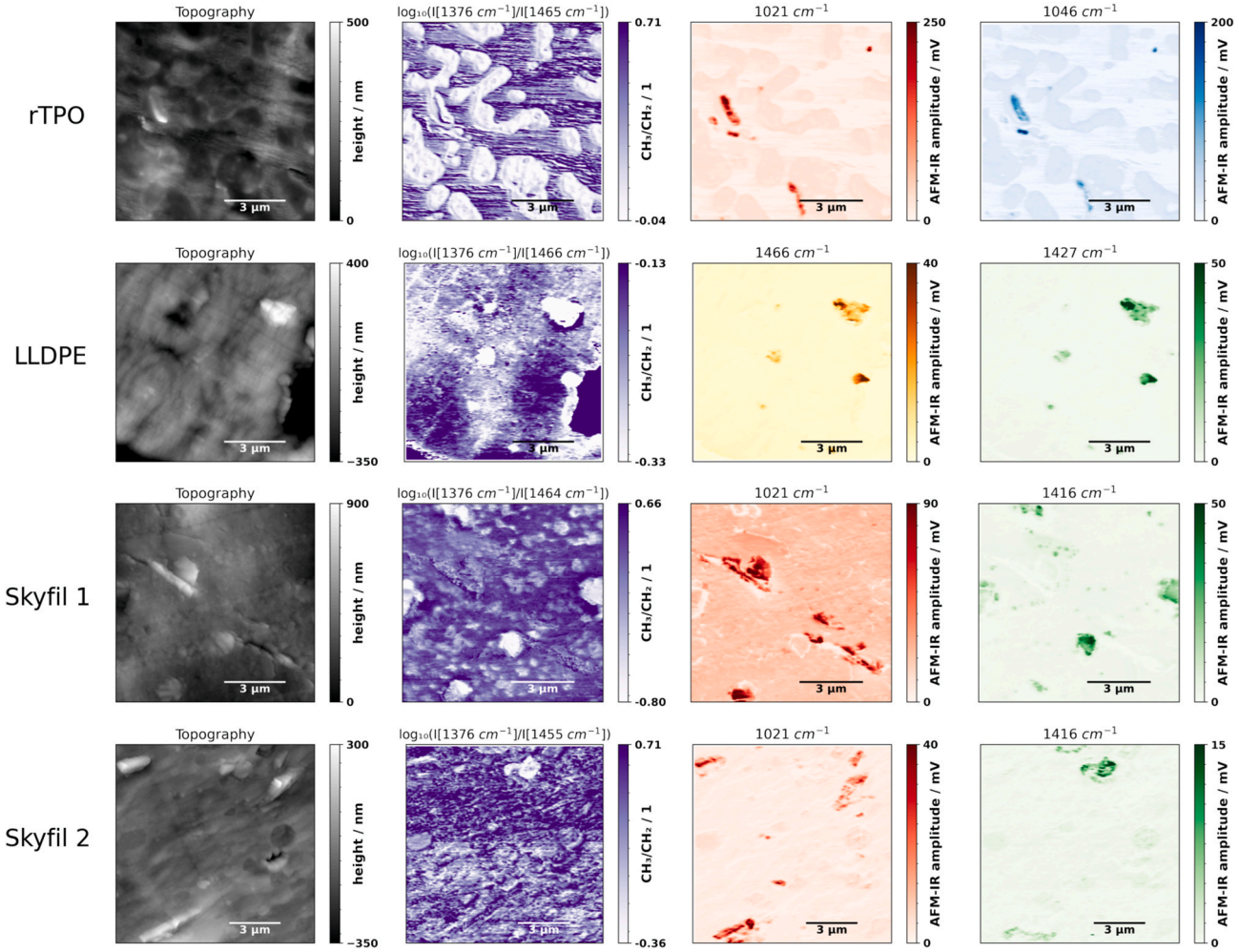

Fig. 4. Topography and chemical maps of the analyzed samples for selected wavenumbers for each of the analyzed samples. Purple corresponds to the ratio of the bands corresponding to deformation vibrations of CH_2 and symmetric deformation of CH_3 groups; Red and blue correspond to the presence of talc; Yellow to CH_2 deformation vibrations; Green indicates the presence of $CaCO_3$. (For interpretation of the references to color in this figure legend, the reader is referred to the Web version of this article.)

higher and lower PE content by comparison of the relative heights of the 1459 cm^{-1} (corresponding to the scissor vibration of $–CH_2$ groups with contributions from asymmetric deformation vibrations of $–CH_3$ groups) and 1376 cm^{-1} peaks (corresponding exclusively to the CH_3 group symmetric vibration band). Moreover, it is also possible to single out locations where talc is present (absorption at 1021 cm^{-1} and 1046 cm^{-1}).

In the case of the recyclates, Skyfil 1 and Skyfil 2 (Fig. 3), the spectra are, as expected, more complex. These recyclates are mixtures of post-consumer and post-industrial materials and contain no virgin material. Both contain talc (1021 cm^{-1}) and $CaCO_3$ (1416 cm^{-1}). As with rTPO it is possible to see differences in PE content for both. An additional band at 1583 cm^{-1} was found in one location which is hardly visible in the bulk FTIR.

3.4. Chemical imaging (step 4)

Once a list of wavenumbers of interest has been compiled, images are taken at each of them (Fig. 1, step 4). Since the AFM-IR signal is transduced as AFM cantilever oscillations that can also be induced or modulated by processes independent of the infrared absorption and laser intensity, it is important to ensure that the AFM-IR amplitude is significantly above the level of such artifacts. A facile way to ensure this is to collect a "mock" AFM-IR image with the laser beam blocked. An example of this can be found in Appendix A. Any features that appear in these mock images that have a magnitude similar those found in actual images point towards issues in the experimental setting (e.g. insufficient tracking of the surface). The image and image ratios obtained from the samples analyzed in this work are presented in Fig. 4. Steps 3 (wavelength selection) and 4 (imaging) may be repeated if some new characteristic is revealed during the imaging that justifies a return to step 3.

3.5. Post-processing (step 5)

The final step involves the interpretation of the acquired data. For single wavelength images, direct interpretation without preprocessing is possible if the signal amplitude for a given wavelength is close to zero everywhere except for a few spots with high absorption. If, however, the imaged wavelength is absorbed in large parts of the image, then evaluation should only be performed via band ratios or multivariate chemometric methods [38,40,67]. Otherwise, the contrast in the image might be dominated by changes in the contact stiffness or the local thermal and mechanical properties rather than absorption. Band ratios are calculated by dividing the pixel values in a chemical image taken at one wavenumber by those measured for another wavenumber. The result is an image that shows the relative changes of the absorption at both signals. The ratio should be unaffected by wavelength independent sample properties, as these are independent of the wavelength.

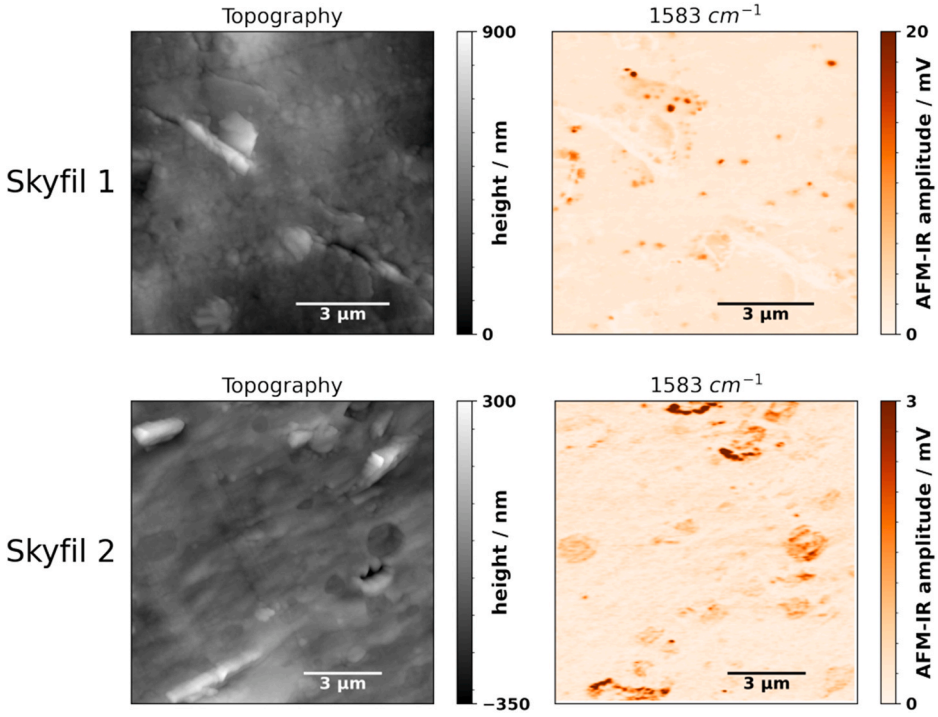

Fig. 5. Topography and chemical maps for further selected wavenumbers for the two recycled samples.

Multivariate methods combine information from a large number of wavelengths via algorithms to either find common trends (e.g., phases) in the data set or to perform quantitation in complex mixtures. A large number of such methods have successfully been applied to mid-IR imaging data, however, the choice of method for a given problem as well as the required preprocessing of data and tuning of hyperparameters is beyond the scope of this article. In this article band ratios (Fig. 4, purple) will be used to aid interpretation.

Independent of whether band ratios or multivariate methods are used some pre-processing is necessary. As the AFM is subject to thermal drift and measurement times for multiple images typically are several hours, images obtained in succession without intentionally moving the sample position show lateral shifts of the sample position. This can be problematic when multiple single wavelength images are combined. For example, band ratios offsets can result in artificially high or low values at the interfaces between phases. Since AFM-IR always acquires an AFM topography image concurrently with the chemical image, the sample topography can be used for correcting sample drifts. The images in Fig. 4 were corrected/registered by using cross correlation in the Fourier domain to determine the shift [68] via the scikit-image python package [60].

After alignment, we calculate the logarithm of the ratio of CH_3 (1376 cm^{-1}) and CH_2 (1466 cm^{-1}or 1455 cm^{-1}) groups intensity and the reveal the distribution of PP and PE in each sample (taking the logarithm ensures that doubling of the intensity in the numerator will lead to an equal but opposite change of the value as a doubling of the intensity of the denominator).

3.6. Interpretation

Below we apply our protocol to several commercial polymers to demonstrate the level of information it can provide.

TPO. For rTPO the CH_3/CH_2 ratio (Fig. 4, purple) allows for a clear visualization of the EPR component (white) inside of the propylene matrix (purple). The core-shell morphology of the rubber particles previously described in literature is well visible with the rigid PP cores inside the rubber particles appearing as purple dots inside the white rubber [50]. Most interestingly, the distribution of the filler, talc (1021 cm^{-1} and 1046 cm^{-1}) is revealed which is not immediately apparent from the topography image: the larger filler particles in this area are present at or close to the interface between PP and EPR (an overlay image for clearer visualization is presented in Appendix A). This could mean that in addition to the nucleating effect and improved impact strength, talc also plays a role in improving the miscibility of PP/EPR blends. Such an effect has been previously observed for talc filled thermoplastic polyurethane/PP blends [69].

LLDPE. In the topography image of the LLDPE sample there are two main features: banded spherulites and a larger particle which IR analysis identifies as $CaCO_3$. Unsurprisingly for a homopolymer, the 1376 cm^{-1} to 1466 cm^{-1} ratio shows no large variations (note that the color bar for the log ratio only covers a delta of 0.2 whereas for the other samples it is three to four times as large) and no particular structures, with the exception of the $CaCO_3$ particles which appear in white. This is due to the $CaCO_3$ band being broad and thus contributing to the 1466 cm^{-1} band and not due to the presence of a different polymer as is the case for rTPO. This effect is identifiable by comparison of the AFM-IR spectra taken in these locations, as well as by comparison of the 1466 cm^{-1} and 1427 cm^{-1} absorption maps, the latter being exclusively due to the presence of $CaCO_3$. $CaCO_3$ is a common filler for LLDPE to reduce melt processing instabilities and increase the tensile yield stress [70,71].

Recyclates. The main distinction between Skyfil 1 and Skyfil 2 is the amount of PE present (approximately 35% PE for Skyfil 1 and 20% for Skyfil 2 according to data provided by PreZero) which is visible when comparing the ratio images for the two recyclates (Fig. 4). As with the LLDPE, care needs to be taken when interpreting the whitest areas of the ratio images. These correspond to $CaCO_3$ particles (as seen in the 1416 cm^{-1} images) and not to PE rich areas. Nonetheless it is possible to see phase separation between the PE and PP components in Skyfil 1. Both polymers contain talc, as well as $CaCO_3$, even though according to information provided by PreZero Polymers, only $CaCO_3$ was intentionally added to Skyfil 1 and talc to Skyfil 2 during the manufacturing process. The amount of filler in recycled samples is thus dependent on the waste material used and may vary, potentially affecting the properties of the final product. For the recyclates an additional band detected in the AFM-

IR spectra was imaged: 1583 cm^{-1} (Fig. 5). Although the band was barely detectable in the bulk FTIR spectra it is widely distributed in both recyclates. In Skyfil 1 it is present as small spots whereas in Skyfil 2 it appears to have a smoother distribution. Since these materials derive from post-consumer plastics they may contain numerous constituents both from the original material (antioxidants, plasticizers, etc.) as well as contaminants picked up during their "former lives" making the identification of what causes this band a challenge. Nonetheless the 1583 band most likely arises from C=C stretching vibration, indicating the presence of unsaturated compounds.

4. Conclusion

A protocol for the fast and reliable identification of the nanostructure and chemical composition of unknown polymer samples is described. Four different commercially polymer samples (two made from virgin materials and two recyclates) were analyzed using the developed protocol. This allowed for the mapping of the distribution of the core-shell rubber particles in the rTPO and the filler distribution in LLDPE. For the two recyclates it was found that both contain talc and $CaCO_3$ as fillers, owing to their previous presence in the waste material. Furthermore, the presence of unsaturated compounds was detected and mapped in both of them.

CRediT author statement

A. Catarina V.D. dos Santos: Conceptualization, Investigation, Visualization, Writing – Original Draft; **Georg Ramer:** Conceptualization, Software, Supervision, Writing – Review & Editing; **Bernhard Lendl:** Resources, Supervision, Funding acquisition, Writing – Review & Editing.

Data availability statement

The raw data required to reproduce these findings are available to download from **https://dx.doi.org/10.5281/zenodo.5607039**.

Declaration of competing interest

The authors declare that they have no known competing financial interests or personal relationships that could have appeared to influence the work reported in this paper.

Acknowledgements

The authors gratefully acknowledge Omya International AG, Omya GmbH and PreZero Polymers for providing the samples used in this study.

The microtome cuts were partially carried out by Martin Binder and Karin Whitmore using facilities at the University Service Centre for Transmission Electron Microscopy (USTEM), TU Wien, Austria.

The authors would also like to thank Walter Schaffer from Borealis for sharing his expertise in microtome cutting of polymer samples.

This work is part of the COMET Centre CHASE. The COMET Centre CHASE is funded within the framework of COMET-Competence Centers for Excellent Technologies by BMVIT, BMDW, the Federal Provinces of Upper Austria and Vienna. The COMET program is run by the Austrian Research Promotion Agency (FFG).

Appendix A. Supplementary data

Supplementary data to this article can be found online at https://doi.org/10.1016/j.polymertesting.2021.107443.

References

[1] S.C. Rasmussen, Revisiting the early history of synthetic polymers: critiques and new insights, Ambix 65 (2018) 356–372, https://doi.org/10.1080/00026980.2018.1512775.

[2] European Comission, COMMUNICATION FROM THE COMMISSION TO THE EUROPEAN PARLIAMENT, THE COUNCIL, 2020. THE EUROPEAN ECONOMIC AND SOCIAL COMMITTEE AND THE COMMITTEE OF THE REGIONS A new Circular Economy Action Plan For a cleaner and more competitive Europe, https://eur-lex.europa.eu/legal-content/EN/TXT/?uri=COM%3A2020%3A98%3AFIN. (Accessed 24 August 2021).

[3] N. Singh, D. Hui, R. Singh, I.P.S. Ahuja, L. Feo, F. Fraternali, Recycling of plastic solid waste: a state of art review and future applications, Compos. B Eng. 115 (2017) 409–422, https://doi.org/10.1016/j.compositesb.2016.09.013.

[4] J.N. Hahladakis, E. Iacovidou, Closing the loop on plastic packaging materials: what is quality and how does it affect their circularity? Sci. Total Environ. 630 (2018) 1394–1400, https://doi.org/10.1016/j.scitotenv.2018.02.330.

[5] L. Mandelkern, The relation between structure and properties of crystalline polymers, Polym. J. 17 (1985) 337–350, https://doi.org/10.1295/polymj.17.337.

[6] S. Crotty, S. Gerişlioğlu, K.J. Endres, C. Wesdemiotis, U.S. Schubert, Polymer architectures via mass spectrometry and hyphenated techniques: a review, Anal. Chim. Acta 932 (2016) 1–21, https://doi.org/10.1016/j.aca.2016.05.024.

[7] S.D. Hanton, Mass spectrometry of polymers and polymer surfaces, Chem. Rev. 101 (2001) 527–570, https://doi.org/10.1021/cr9901081.

[8] C. Wesdemiotis, Multidimensional mass spectrometry of synthetic polymers and advanced materials, Angew. Chem. Int. Ed. 56 (2017) 1452–1464, https://doi.org/10.1002/anie.201607003.

[9] N.S. Murthy, H. Minor, General procedure for evaluating amorphous scattering and crystallinity from X-ray diffraction scans of semicrystalline polymers, Polymer 31 (1990) 996–1002, https://doi.org/10.1016/0032-3861(90)90243-R.

[10] M.J. Kory, M. Wörle, T. Weber, P. Payamyar, S.W. van de Poll, J. Dshemuchadse, N. Trapp, A.D. Schlüter, Gram-scale synthesis of two-dimensional polymer crystals and their structure analysis by X-ray diffraction, Nat. Chem. 6 (2014) 779–784, https://doi.org/10.1038/nchem.2007.

[11] D. Kim, J.S. Lee, C.M.F. Barry, J.L. Mead, Microscopic measurement of the degree of mixing for nanoparticles in polymer nanocomposites by TEM images, Microsc. Res. Tech. 70 (2007) 539–546, https://doi.org/10.1002/jemt.20478.

[12] F.M. Mirabella, N. Dioh, C.G. Zimba, Theoretical analysis and experimental characterization of the TPO/adhesion promoter/paint interface of painted thermoplastic polyolefins (TPO), Polym. Eng. Sci. 40 (2000) 2000–2006, https://doi.org/10.1002/pen.11332.

[13] M.A. Ghalia, A. Hassan, A. Yussuf, Mechanical and thermal properties of calcium carbonate-filled PP/LLDPE composite, J. Appl. Polym. Sci. 121 (2011) 2413–2421, https://doi.org/10.1002/app.33570.

[14] J.P. Da Costa, A.R. Nunes, P.S.M. Santos, A.V. Girão, A.C. Duarte, T. Rocha-Santos, Degradation of polyethylene microplastics in seawater: insights into the environmental degradation of polymers, Journal of Environmental Science and Health, Part A. 53 (2018) 866–875, https://doi.org/10.1080/10934529.2018.1455381.

[15] V.I. Raman, G.R. Palmese, Nanoporous thermosetting polymers, Langmuir 21 (2005) 1539–1546, https://doi.org/10.1021/la048393t.

[16] C.G. Schirmeister, S. Schächtele, Y. Keßler, T. Hees, R. Köhler, K. Schmitz, E. H. Licht, R. Muelhaupt, Low warpage nanophase-separated polypropylene/olefinic elastomer reactor blend composites with digitally tuned glass fiber orientation by extrusion-based additive manufacturing, ACS Appl. Polym. Mater. 3 (2021) 2070–2081, https://doi.org/10.1021/acsapm.1c00119.

[17] P. Enrique-Jimenez, J.F. Vega, J. Martínez-Salazar, F. Ania, A. Flores, Mapping the mechanical properties of Poly(3-hydroxybutyrate-co-3-hydroxyvalerate) banded spherulites by nanoindentation, Polymers 8 (2016) 358, https://doi.org/10.3390/polym8100358.

[18] J. Xu, B.-H. Guo, Z.-M. Zhang, J.-J. Zhou, Y. Jiang, S. Yan, L. Li, Q. Wu, G.-Q. Chen, J.M. Schultz, Direct AFM observation of crystal twisting and organization in banded spherulites of chiral Poly(3-hydroxybutyrate-co-3-hydroxyhexanoate), Macromolecules 37 (2004) 4118–4123, https://doi.org/10.1021/ma0499122.

[19] E. Karavas, M. Georgarakis, A. Docoslis, D. Bikiaris, Combining SEM, TEM, and micro-Raman techniques to differentiate between the amorphous molecular level dispersions and nanodispersions of a poorly water-soluble drug within a polymer matrix, Int. J. Pharm. 340 (2007) 76–83, https://doi.org/10.1016/j.ijpharm.2007.03.037.

[20] J. Hu, J. Wang, M. Wang, Y. Ozaki, H. Sato, J. Zhang, Investigation of crystallization behavior of asymmetric PLLA/PDLA blend using Raman Imaging measurement, Polymer 172 (2019) 1–6, https://doi.org/10.1016/j.polymer.2019.03.049.

[21] J. Cheng, X. Yang, L. Dong, Z. Yuan, W. Wang, S. Wu, S. Chen, G. Zheng, W. Zhang, D. Zhang, H. Wang, Effective nondestructive evaluations on UHMWPE/Recycled-PA6 blends using FTIR imaging and dynamic mechanical analysis, Polym. Test. 59 (2017) 371–376, https://doi.org/10.1016/j.polymertesting.2017.02.021.

[22] T. Mukherjee, M.J. Tobin, L. Puskar, M.-A. Sani, N. Kao, R.K. Gupta, M. Pannirselvam, N. Quazi, S. Bhattacharya, Chemically imaging the interaction of acetylated nanocrystalline cellulose (NCC) with a polylactic acid (PLA) polymer matrix, Cellulose 24 (2017) 1717–1729, https://doi.org/10.1007/s10570-017-1217-x.

[23] R. Xie, B. Qu, Expandable graphite systems for halogen-free flame-retarding of polyolefins. II. Structures of intumescent char and flame-retardant mechanism, J. Appl. Polym. Sci. 80 (2001) 1190–1197, https://doi.org/10.1002/app.1203.

[24] A. Dazzi, PhotoThermal induced resonance. Application to infrared spectromicroscopy, in: S. Volz (Ed.), Thermal Nanosystems and Nanomaterials, Springer, Berlin, Heidelberg, 2009, pp. 469–503, https://doi.org/10.1007/978-3-642-04258-4_16.

[25] P. Lasch, D. Naumann, Spatial resolution in infrared microspectroscopic imaging of tissues, Biochim. Biophys. Acta Biomembr. 1758 (2006) 814–829, https://doi.org/10.1016/j.bbamem.2006.06.008.

[26] A. Dazzi, F. Glotin, R. Carminati, Theory of infrared nanospectroscopy by photothermal induced resonance, J. Appl. Phys. 107 (2010) 124519, https://doi.org/10.1063/1.3429214.

[27] K. Wieland, G. Ramer, V.U. Weiss, G. Allmaier, B. Lendl, A. Centrone, Nanoscale chemical imaging of individual chemotherapeutic cytarabine-loaded liposomal nanocarriers, Nano Research 12 (2019) 197–203, https://doi.org/10.1007/s12274-018-2202-x.

[28] G.J. Verbiest, M.J. Rost, Beating beats mixing in heterodyne detection schemes, Nat. Commun. 6 (2015) 6444, https://doi.org/10.1038/ncomms7444.

[29] D. Kurouski, A. Dazzi, R. Zenobi, A. Centrone, Infrared and Raman chemical imaging and spectroscopy at the nanoscale, Chem. Soc. Rev. 49 (2020) 3315–3347, https://doi.org/10.1039/C8CS00916C.

[30] V.W. Or, A.D. Estillore, A.V. Tivanski, V.H. Grassian, Lab on a tip: atomic force microscopy – photothermal infrared spectroscopy of atmospherically relevant organic/inorganic aerosol particles in the nanometer to micrometer size range, Analyst 143 (2018) 2765–2774, https://doi.org/10.1039/C8AN00171E.

[31] D. Khanal, J. Zhang, W.-R. Ke, M.M. Banaszak Holl, H.-K. Chan, Bulk to nanometer-scale infrared spectroscopy of Pharmaceutical dry Powder aerosols, Anal. Chem. 92 (2020) 8323–8332, https://doi.org/10.1021/acs.analchem.0c00729.

[32] V.J. Rao, M. Matthiesen, K.P. Goetz, C. Huck, C. Yim, R. Siris, J. Han, S. Hahn, U.H. F. Bunz, A. Dreuw, G.S. Duesberg, A. Pucci, J. Zaumseil, AFM-IR and IR-SNOM for the characterization of small molecule organic semiconductors, J. Phys. Chem. C 124 (2020) 5331–5344, https://doi.org/10.1021/acs.jpcc.9b11056.

[33] J. Mathurin, E. Pancani, A. Deniset-Besseau, K. Kjoller, C.B. Prater, R. Gref, A. Dazzi, How to unravel the chemical structure and component localization of individual drug-loaded polymeric nanoparticles by using tapping AFM-IR, Analyst 143 (2018) 5940–5949, https://doi.org/10.1039/C8AN01239C.

[34] A.M. Katzenmeyer, J. Canivet, G. Holland, D. Farrusseng, A. Centrone, Assessing chemical heterogeneity at the nanoscale in mixed-ligand metal–organic frameworks with the PTIR technique, Angew. Chem. Int. Ed. 53 (2014) 2852–2856, https://doi.org/10.1002/anie.201309295.

[35] X. Ma, V. Beltran, G. Ramer, G. Pavlidis, D.Y. Parkinson, M. Thoury, T. Meldrum, A. Centrone, B.H. Berrie, Revealing the distribution of metal carboxylates in oil paint from the micro- to nanoscale, Angew. Chem. Int. Ed. 58 (2019) 11652–11656, https://doi.org/10.1002/anie.201903553.

[36] T. Dou, Z. Li, J. Zhang, A. Evilevitch, D. Kurouski, Nanoscale structural characterization of individual viral particles using atomic force microscopy infrared spectroscopy (AFM-IR) and tip-enhanced Raman spectroscopy (TERS), Anal. Chem. 92 (2020) 11297–11304, https://doi.org/10.1021/acs.analchem.0c01971.

[37] D. Khanal, R.Y.K. Chang, S. Morales, H.-K. Chan, W. Chrzanowski, High resolution nanoscale probing of bacteriophages in an inhalable dry Powder formulation for Pulmonary infections, Anal. Chem. 91 (2019) 12760–12767, https://doi.org/10.1021/acs.analchem.9b02282.

[38] D. Perez-Guaita, K. Kochan, M. Batty, C. Doerig, J. Garcia-Bustos, S. Espinoza, D. McNaughton, P. Heraud, B.R. Wood, Multispectral atomic force microscopy-infrared nano-imaging of malaria infected red blood cells, Anal. Chem. 90 (2018) 3140–3148, https://doi.org/10.1021/acs.analchem.7b04318.

[39] L. Baldassarre, V. Giliberti, A. Rosa, M. Ortolani, A. Bonamore, P. Baiocco, K. Kjoller, P. Calvani, A. Nucara, Mapping the amide I absorption in single bacteria and mammalian cells with resonant infrared nanospectroscopy, Nanotechnology 27 (2016), 075101, https://doi.org/10.1088/0957-4484/27/7/075101.

[40] A.C.V.D. dos Santos, R. Heydenreich, C. Derntl, A.R. Mach-Aigner, R.L. Mach, G. Ramer, B. Lendl, Nanoscale infrared spectroscopy and chemometrics enable detection of intracellular protein distribution, Anal. Chem. 92 (2020) 15719–15725, https://doi.org/10.1021/acs.analchem.0c02228.

[41] P.N. Tri, R.E. Prud'homme, Nanoscale lamellar assembly and segregation mechanism of Poly(3-hydroxybutyrate)/Poly(ethylene glycol) blends, Macromolecules 51 (2018) 181–188, https://doi.org/10.1021/acs.macromol.7b02019.

[42] P. Nguyen Tri, R.E. Prud'homme, Crystallization and segregation behavior at the submicrometer scale of PCL/PEG blends, Macromolecules 51 (2018) 7266–7273, https://doi.org/10.1021/acs.macromol.8b01503.

[43] M.A. Rickard, G.F. Meyers, B.M. Habersberger, C.W. Reinhardt, J.J. Stanley, Nanoscale chemical imaging of a deuterium-labeled polyolefin copolymer in a polyolefin blend by atomic force microscopy-infrared spectroscopy, Polymer 129 (2017) 247–251, https://doi.org/10.1016/j.polymer.2017.09.045.

[44] P. Nguyen-Tri, R.E. Prud'homme, Nanoscale analysis of the photodegradation of polyester fibers by AFM-IR, J. Photochem. Photobiol. Chem. 371 (2019) 196–204, https://doi.org/10.1016/j.jphotochem.2018.11.017.

[45] H. Luo, Y. Xiang, Y. Li, Y. Zhao, X. Pan, Photocatalytic aging process of Nano-TiO2 coated polypropylene microplastics: combining atomic force microscopy and infrared spectroscopy (AFM-IR) for nanoscale chemical characterization, J. Hazard Mater. 404 (2021) 124159, https://doi.org/10.1016/j.jhazmat.2020.124159.

[46] H. McDonald, S. Morsch, S.M. Rowland, Chemical analysis of tree growth in epoxy resin using AFM-IR spectroscopy, IEEE Trans. Dielectr. Electr. Insul. 27 (2020) 773–781, https://doi.org/10.1109/TDEI.2019.008573.

[47] F. Cavezza, S. Pletincx, R.I. Revilla, J. Weaytens, M. Boehm, H. Terryn, T. Hauffman, Probing the metal oxide/polymer molecular hybrid interfaces with nanoscale resolution using AFM-IR, J. Phys. Chem. C 123 (2019) 26178–26184, https://doi.org/10.1021/acs.jpcc.9b04522.

[48] N. Baden, Novel method for high-spatial-resolution chemical analysis of buried polymer-metal interface: atomic force microscopy-infrared (AFM-IR) spectroscopy with low-angle microtomy, Appl. Spectrosc. 75 (2021) 901–910, https://doi.org/10.1177/00037028211007187.

[49] F. Tang, P. Bao, Z. Su, Analysis of nanodomain composition in high-impact polypropylene by atomic force microscopy-infrared, Anal. Chem. 88 (2016) 4926–4930, https://doi.org/10.1021/acs.analchem.6b00798.

[50] F. Tang, P. Bao, A. Roy, Y. Wang, Z. Su, In-situ spectroscopic and thermal analyses of phase domains in high-impact polypropylene, Polymer 142 (2018) 155–163, https://doi.org/10.1016/j.polymer.2018.03.037.

[51] Plastics - the facts 2020, PlasticsEurope, n.d, https://www.plasticseurope.org/en/resources/publications/4312-plastics-facts-2020. (Accessed 9 August 2021).

[52] W. Posch, 3 - polyolefins, in: M. Kutz (Ed.), Applied Plastics Engineering Handbook, William Andrew Publishing, Oxford, 2011, pp. 23–48, https://doi.org/10.1016/B978-1-4377-3514-7.10003-0.

[53] L.K. Massey, Chapter 70 - olefinic thermoplastic elastomers (TPO), in: L.K. Massey (Ed.), Permeability Properties of Plastics and Elastomers, second ed., William Andrew Publishing, Norwich, NY, 2003, pp. 421–425, https://doi.org/10.1016/B978-188420797-6.50072-3.

[54] P. Galli, The reactor granule technology: a revolutionary approach to polymer blends and alloys, Macromol. Symp. 78 (1994) 269–284, https://doi.org/10.1002/masy.19940780123.

[55] A. Ghanbari, E. Behzadfar, M. Arjmand, Properties of talc filled reactor-made thermoplastic polyolefin composites, J. Polym. Res. 26 (2019) 241, https://doi.org/10.1007/s10965-019-1902-6.

[56] R. Sadiku, D. Ibrahim, O. Agboola, S.J. Owonubi, V.O. Fasiku, W.K. Kupolati, T. Jamiru, A.A. Eze, O.S. Adekomaya, K. Varaprasad, S.C. Agwuncha, A.B. Reddy, B. Manjula, B. Oboirien, C. Nkuna, M. Dludlu, A. Adeyeye, T.S. Osholana, G. Phiri, O. Durowoju, P.A. Olubambi, F. Biotidara, M. Ramakokovhu, B. Shongwe, V. Ojijo, 15 - automotive components composed of polyolefins, in: S.C.O. Ugbolue (Ed.), Polyolefin Fibres, second ed., Woodhead Publishing, 2017, pp. 449–496, https://doi.org/10.1016/B978-0-08-101132-4.00015-1.

[57] D.M. Simpson, G.A. Vaughan, Ethylene polymers, LLDPE, in: Encyclopedia of Polymer Science and Technology, American Cancer Society, 2001, https://doi.org/10.1002/0471440264.pst122.

[58] T.K. Goswami, S. Mangaraj, 8 - advances in polymeric materials for modified atmosphere packaging (MAP), in: J.-M. Lagarón (Ed.), Multifunctional and Nanoreinforced Polymers for Food Packaging, Woodhead Publishing, 2011, pp. 163–242, https://doi.org/10.1533/9780857092786.1.163.

[59] S.E. Selke, R.J. Hernandez, Packaging: polymers in flexible packaging, in: K.H. J. Buschow, R.W. Cahn, M.C. Flemings, B. Ilschner, E.J. Kramer, S. Mahajan, P. Veyssière (Eds.), Encyclopedia of Materials: Science and Technology, Elsevier, Oxford, 2001, pp. 6652–6656, https://doi.org/10.1016/B0-08-043152-6/01176-1.

[60] S. van der Walt, J.L. Schönberger, J. Nunez-Iglesias, F. Boulogne, J.D. Warner, N. Yager, E. Gouillart, T. Yu, The scikit-image contributors, scikit-image: image processing in Python, PeerJ 2 (2014) e453, https://doi.org/10.7717/peerj.453.

[61] S. Morsch, S.B. Lyon, S. Edmondson, S.R. Gibbon, Reflectance in AFM-IR: implications for interpretation and remote analysis of the buried interface, Anal. Chem. (2020), https://doi.org/10.1021/acs.analchem.9b05793.

[62] S.N. Magonov, D.H. Reneker, Characterization of polymer surfaces with atomic force microscopy, Annu. Rev. Mater. Sci. 27 (1997) 175–222, https://doi.org/10.1146/annurev.matsci.27.1.175.

[63] J.M. Chalmers, N.J. Everall, Polymer analysis and characterization by FTIR, FTIR-microscopy, Raman spectroscopy and chemometrics, Int. J. Polym. Anal. Char. 5 (1999) 223–245, https://doi.org/10.1080/10236669908009739.

[64] I. Pumure, S. Ford, J. Shannon, C. Kohen, A. Mulcahy, K. Frank, S. Sisco, N. Chaukura, Analysis of ATR-FTIR absorption-reflection data from 13 polymeric fabric materials using chemometrics, Am. J. Anal. Chem. (2015) 305, https://doi.org/10.4236/ajac.2015.64029, 06.

[65] J. McGann, M. Willans, G. Sauzier, M.J. Hackett, S.W. Lewis, J. McGinn, T. Trubshoe, W. van Bronswijk, Investigating diversity in polymer-based identity cards using ATR-FTIR spectroscopy and chemometrics, Forensic Sci. Int.: Report 2 (2020) 100149, https://doi.org/10.1016/j.fsir.2020.100149.

[66] Y.-S. Lo, N.D. Huefner, W.S. Chan, P. Dryden, B. Hagenhoff, T.P. Beebe, Organic and inorganic contamination on commercial AFM cantilevers, Langmuir 15 (1999) 6522–6526, https://doi.org/10.1021/la990371x.

[67] G. Ramer, V.A. Aksyuk, A. Centrone, Quantitative chemical analysis at the nanoscale using the PTIR technique, Anal. Chem. 89 (2017) 13524–13531, https://doi.org/10.1021/acs.analchem.7b03878.

[68] M. Guizar-Sicairos, S.T. Thurman, J.R. Fienup, Efficient subpixel image registration algorithms, Opt. Lett., OL. 33 (2008) 156–158, https://doi.org/10.1364/OL.33.000156.

[69] E. Govorčin Bajsić, V. Rek, I. Ćosić, Preparation and characterization of talc filled thermoplastic polyurethane/polypropylene blends, Journal of Polymers (2014), e289283, https://doi.org/10.1155/2014/289283, 2014.

[70] M. Barczewski, K. Lewandowski, M. Schmidt, M. Szostak, Melt fracture and rheology of linear low density polyethylene - calcium carbonate composites, Polym. Eng. Sci. 57 (2017) 998–1004, https://doi.org/10.1002/pen.24477.

[71] J. Móczó, B. Pukánszky, Polymer micro and nanocomposites: structure, interactions, properties, J. Ind. Eng. Chem. 14 (2008) 535–563, https://doi.org/10.1016/j.jiec.2008.06.011.